JACS
JOURNAL OF THE AMERICAN CHEMICAL SOCIETY
pubs.acs.org/JACS
Article

Capillary-Assisted Molecular Pendulum Bioanalysis

Hossein Zargartalebi, Hanie Yousefi, Connor D. Flynn, Surath Gomis, Jagotamoy Das, Tiana L. Young, Emily Chien, Samira Mubareka, Allison McGeer, Hansen Wang, Edward H. Sargent, Amir Sanati Nezhad,* and Shana O. Kelley*

Cite This: J. Am. Chem. Soc. 2022, 144, 18338−18349
Read Online

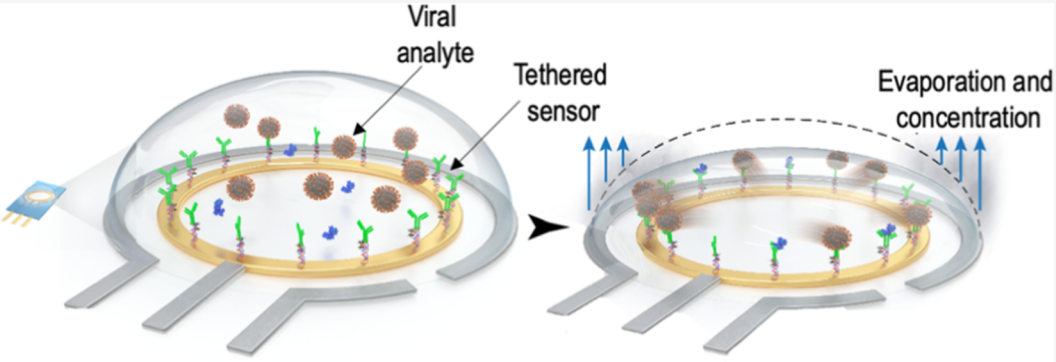

ABSTRACT: The development of robust biosensing strategies that can be easily implemented in everyday life remains a challenge for the future of modern biosensor research. While several reagentless approaches have attempted to address this challenge, they often achieve user-friendliness through sacrificing sensitivity or universality. While acceptable for certain applications, these trade-offs hinder the widespread adoption of reagentless biosensing technologies. Here, we report a novel approach to reagentless biosensing that achieves high sensitivity, rapid detection, and universality using the SARS-CoV-2 virus as a model target. Universality is achieved by using nanoscale molecular pendulums, which enables reagentless electrochemical biosensing through a variable antibody recognition element. Enhanced sensitivity and rapid detection are accomplished by incorporating the coffee-ring phenomenon into the sensing scheme, allowing for target preconcentration on a ring-shaped electrode. Using this approach, we obtained limits of detection of 1 fg/mL and 20 copies/mL for the SARS-CoV-2 nucleoproteins and viral particles, respectively. In addition, clinical sample analysis showed excellent agreement with Ct values from PCR-positive SARS-CoV-2 patients.

INTRODUCTION

The modern biosensing landscape, while rich in new and exciting detection mechanisms, frequently suffers from an inability to translate techniques to non-laboratory settings.[1] As such, considerable efforts have aimed to develop detection schemes that are simple, reagentless, and easily implementable on a broad scale.[2] Traditional reagentless approaches, such as enzymatic test strips[3] and lateral flow assays,[4] have dominated the commercial biosensing market for the last half a century; however, these sensing approaches are often inherently restricted to specific analytes and possess relatively low sensitivities.[5] The development of novel, self-contained biosensing mechanisms with high sensitivity and universal analyte selectivity remains a key requirement in the evolution of biosensing, beyond simple metabolite detection and toward more sensitive and adaptable biosensing technologies.

The importance of reagentless assays has been recently reinforced by the ongoing severe acute respiratory syndrome coronavirus 2 (SARS-CoV-2) pandemic, which has necessitated the development of point-of-care (POC) viral testing methods.[6,7] Nucleic acid amplification-based tests have been the gold standard for SARS-CoV-2 diagnosis, but their lengthy processing time and the need for expensive equipment and highly qualified technicians make them ill-suited for rapid POC and mass screening.[8,9] In an attempt to supplement these amplification assays, POC antigen tests, which target viral proteins and provide results within minutes, have been brought to the market; however, these tests are mainly lateral flow assays that report only qualitative information and have suboptimal sensitivities.[10] Many other SARS-CoV-2 biosensing strategies have been proposed using various optical and electrochemical biosensing approaches;[11−16] these tests provide quantitative

Received: June 12, 2022
Published: September 29, 2022

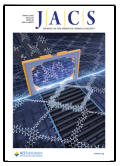

https://doi.org/10.1021/jacs.2c06192
J. Am. Chem. Soc. 2022, 144, 18338−18349

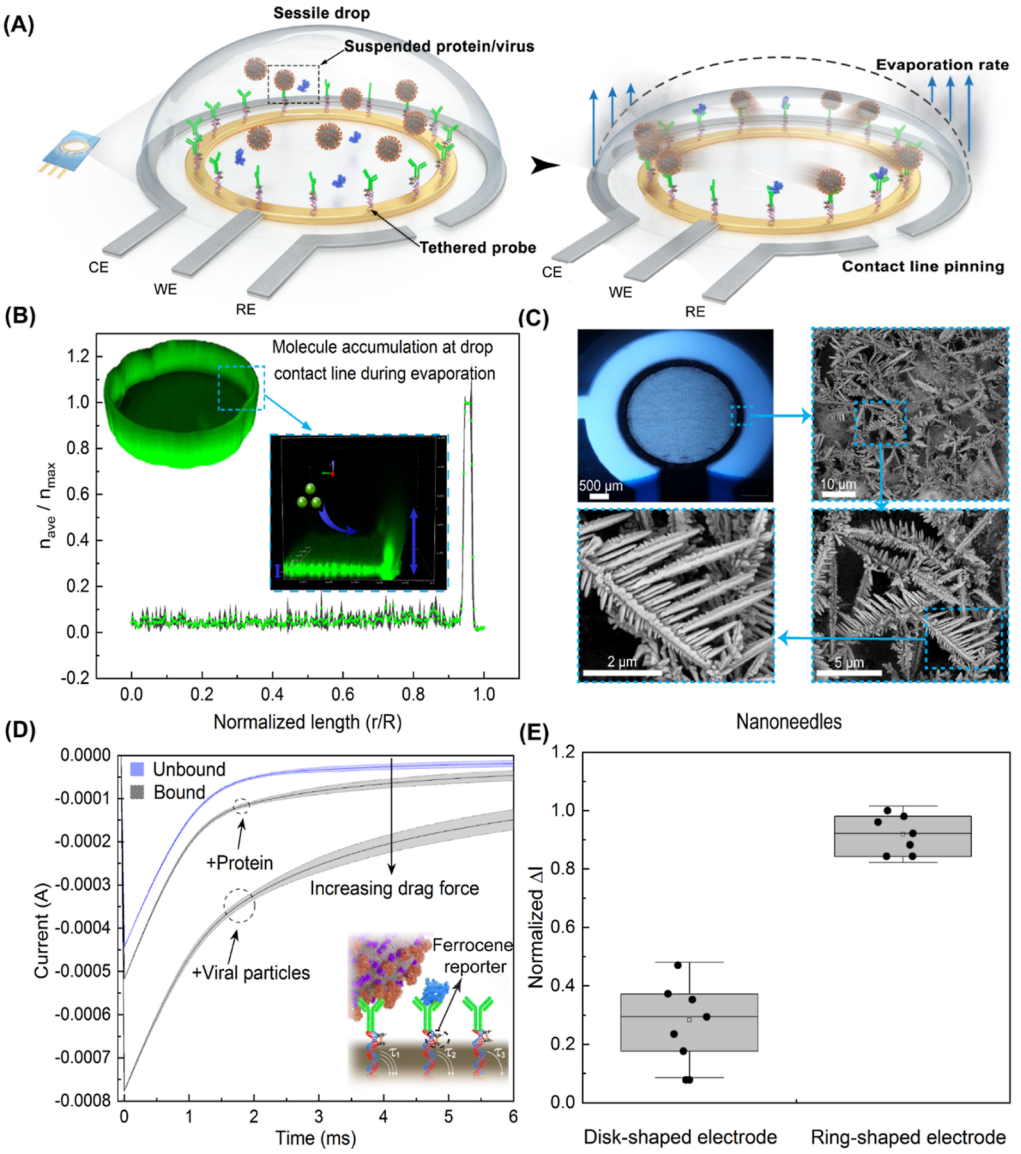

Figure 1. | Coffee-ring phenomenon and sensing approach. (A) Coffee-ring mechanism leads to molecule accumulation at the pinned contact line, such that the density of molecules is significantly higher at the droplet perimeter compared to the droplet center. The reagentless detection approach uses the nanoscale molecular pendulum (NMP) methodology. A protein-binding NMP is constructed using double-stranded DNA, where one strand contains a ligand specific for Spike 1 and Nucleocapsid recombinant proteins and the other contains a terminal ferrocene redox reporter, which is conjugated to the amine-terminated DNA sequences. A positive potential applied to the biosensor transports the NMP to the electrode surface, which oxidizes the ferrocene and enables NMP measurement. (B) Molecule accumulation at the contact line, representing a very high concentration of molecules at the ring working electrode compared to the droplet center. (C) Laser engraved screen-printed gold electrode, fabricated into a ring-like biosensor to decrease the active surface area of the working electrode and contribute to its increased sensitivity. Scanning electron microscopy (SEM) micrographs of three-dimensional gold nanoneedles (GNNs) decorate the electrode surface and increase its surface area. (D) Experimental time-dependent current transient, which shows binding-induced modulation of NMP transport, adopting chronoamperometry (potential step of +300 mV) for unbound (blue line) and bound N-protein (1 pg mL^{-1}) as well as pseudotyped SARS-CoV-2 virus (5,000 copies mL^{-1}) in saliva (gray lines). The shaded lines represent the standard deviation, with $n = 5$ for each trace. (E) Comparing the signals for the ring-like electrode (coffee-ring) and a disc-like electrode (no coffee-ring) with the same surface area, showing signal enhancement in the presence of the coffee-ring effect.

information and improved sensitivities but remain difficult to implement due to the reagent-dependent nature of their reaction schemes. To effectively assess and control SARS-CoV-2 transmission during the post-pandemic where there is a significant drop in RT-PCR testing in many countries, there is a need for universal biosensing approaches that can combine both high sensitivity and rapid, reagent-free detection to address these societal needs.

Recently, we introduced the concept of the nanoscale molecular pendulum (NMP) as a mediator for reagentless electrochemical biosensing.[17] NMPs consist of antibody-conjugated DNA covalently immobilized on an electrode surface. Upon application of a sufficiently positive potential, the negatively charged DNA descends toward the electrode surface, allowing for oxidation of a terminal ferrocene molecule. NMP-based detection is achieved through differential pendulum migration based on whether the target is bound to the adjoining antibody, such that target−antibody complexes move slower and delay ferrocene oxidation. Chronoamperometry (CA) is employed to both provide the potential change and track

https://doi.org/10.1021/jacs.2c06192
J. Am. Chem. Soc. 2022, 144, 18338−18349

ferrocene oxidation. Because this approach relies solely on hydrodynamic differences, it circumvents the need for additional reagents and therefore enables rapid and reagentless detection. A subsequent follow-up study demonstrated that the NMP approach could successfully detect both SARS-CoV-2 spike proteins and viral particles with a high degree of accuracy.[18] While this previous work served as an excellent preliminary study, it remains possible to push this methodology even further toward heightened sensitivity and improved functionality.

When it comes to detecting minute quantities of an analyte, preconcentration is a common approach to controllably direct the analyte toward the biosensing area, which induces improved sensitivity. However, most commonly employed preconcentration methods (e.g., extractions, isotachophoresis) typically involve time-consuming external processes and reagent involvement steps that do not lend themselves to rapid POC sensing.[19,20] To overcome this barrier and enable reagentless preconcentration, a unique physical phenomenon—known as the coffee ring effect—was explored for the first time in this work. The coffee ring effect describes the tendency of solids suspended in solution to accumulate along the perimeter of an evaporating droplet.[21−23] It occurs as the outer contact lines of a droplet are pinned to the surface on which the drop rests, causing the area in contact with the surface to remain constant. Because evaporation is most pronounced along the edges of the drop, a capillary-like flow of internal fluid constantly moves toward the droplet edge to maintain its shape. This constant outward flow of fluid is responsible for concentrating dissolved or suspended solids along the outer ridge. While most research efforts involving this phenomenon have looked at suppressing its effects,[23] the natural capillary flow involved in the coffee-ring effect may be highly beneficial when properly implemented in some applications.[24]

Here, we expand upon the previously reported NMP biosensing approach to develop a reagentless SARS-CoV-2 biosensor with improved response time and sensitivity of the biosensor. To achieve this, we exploit the natural capillary flow offered by the coffee ring effect to develop the capillary-assisted molecular pendulum assay (CAMPA), which provides enhanced concentration of the analyte and improved sensitivity without a need for any external manipulation. The desired uniform ring-shaped sensing electrodes were fabricated through laser removal of the screen-printed electrode interior. The electrode ring's thickness and gold nanostructure were carefully optimized to achieve maximal sensitivity.[25] By incorporating the coffee ring effect with NMP-based biosensing, we achieved significantly enhanced sensitivity toward both the target protein and the virus itself, which was demonstrated with clinical SARS-CoV-2 samples. In addition to experimental results, a comprehensive theoretical study was conducted to verify and support the robustness of this coffee-ring preconcentration approach.

RESULTS AND DISCUSSIONS

Biosensing Mechanism. Inside an evaporating sessile droplet, there is a constant capillary force directed toward the contact line due to the non-equilibrium evaporation rate along the liquid−vapor interface. This radially outward force carries the solution, along with its suspended particles, to the edge of the droplet—a phenomenon known as the coffee-ring effect.[21] We sought to take advantage of this phenomenon by designing a highly sensitive and rapid monitoring system for the detection of target analytes in bodily fluid samples. To achieve this, screen-printed electrodes (SPEs) were engraved using a CO_2 laser cutter to form ring-shaped working electrodes with an appropriate thickness (Figures S1 and 1A, left). The target molecules are suspended in the droplet, cast on the electrode, migrate to the droplet edge, and are captured on the ring-shaped electrode (Figure 1A). A reagentless method based on molecular pendulum dynamics was used for electrochemical biosensing, offering simple-to-use, sensitive, and real-time monitoring of target molecules.[17] Notably, the conventional SPEs possess a large surface area, which is not appropriate to address the needs of molecular pendulum biosensing that requires small electrode sizes to collect and detect minute concentrations of the analyte in the sample (Figure S1).

To analyze the influence of the coffee-ring effect, we measured the average concentration gradient of fluorescent molecules, with a size comparable to a viral particle, deposited along the droplet radius (Figure 1B). We observed that the concentration of molecules at the contact line is approximately 12 times higher than that of the droplet center (Figure 1B), confirming the occurrence of preconcentrating the molecules on the droplet perimeter. The dynamic contact angle and sequential images of the evaporating droplet on top of the electrode were monitored to ensure the sample contact line remained pinned during evaporation (Figure S2). We electrodeposited gold nanoneedles (GNN) on the working electrode to increase the biosensor's sensitivity (Figure 1C). The electrode surface was electrochemically cleaned before and after GNN deposition to minimize surface contamination and to ensure repeatability and reliability of the electrode signals in the downstream sensing investigations (Figure S3). It is worth mentioning that this nano-coated electrode remains stable for at least 1 month at room temperature, as confirmed by cyclic voltammetry (Figure S4). Next, we immobilized the probe on the GNNs by incubating a droplet of molecular pendulum constructs ($P1$ + $P2$) on the working electrode. After incubation and buffer exchange to remove unbound particles, we introduced the sample solution spiked with the target analyte (protein and virus). Preconcentrating the sample starts immediately with the evaporation of the droplet on the ring electrode due to the non-uniform evaporation rate along the liquid−vapor interface, such that particles are directed by capillary flow toward the ring edge due to the coffee-ring effect (Figure 1A, right).

Target Detection on the Coffee-Ring Electrodes. CA measurements of the molecular pendulum confirm the presence of the target (nucleocapsid protein or SARS-CoV-2 virus) in samples through the change in the current decay rate. When there is no attachment (unbound) of the NMP to the target, the current decay rate is extremely fast, but the rate slows significantly when the NMP is bound to the target as the change in the mass of the molecular pendulum leads to an increased drag force and slower current decay rates. The difference in the current values (ΔI) at a certain time (i.e., 2 ms) is used for the detection of the target. Moreover, the target size directly affects the time required for the NMP to travel to the electrode surface, which differentiates between the protein-bound and virus-bound states (Figure 1D). Square wave voltammetry (SWV), step 4 mV, amplitude 25 mV, and frequency 60 Hz, in 0.1× phosphate buffer saline (PBS) is also used to confirm ferrocene peak change after protein binding (Figure S5). The ferrocene peak is commonly between 0.2 and 0.35 V. As we tested it in 0.1× PBS buffer, there is no other electroactive substances/electrolyte to oxidize/reduce in this potential range. We observed no peak when testing the same sensors without the ferrocene redox in 0.1× PBS to ensure the

https://doi.org/10.1021/jacs.2c06192
J. Am. Chem. Soc. 2022, 144, 18338−18349

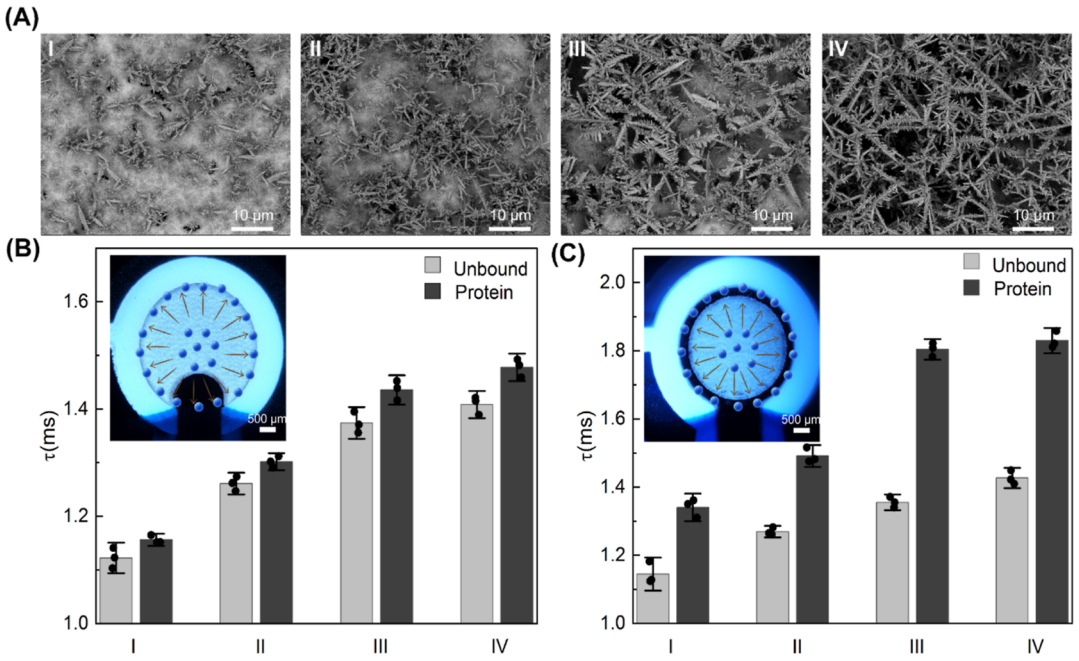

Figure 2. | Tuning the sensitivity of the biosensor by changing surface area and morphology. (A), SEM micrographs of various gold nanostructures with different surface areas and morphologies. (B,C), Comparing the time (τ) required for the NMP to reach the electrode surface for a disk-like electrode (B) and a ring-like electrode (C) with various nanocomposites, considering unbound and protein-bound configurations. It is evident that the difference between the two configurations is insignificant for the disk-like electrode with respect to the ring-like electrode.

peak is related to the Fc redox (Figure S6). ΔI of the ring electrodes, which strongly correlates with the resolution of the system, is five times larger than ΔI of traditional small disk-shaped electrodes with the same surface area as the ring electrodes (Figure 1E). This significant difference is understandable as a high percentage of the target proteins do not contact the tethered probes on the electrode surface when the electrode shape is like a disc, which further highlights the strength of the coffee-ring effect, enabling sample preconcentration on ring-shaped electrodes. The reason behind the 5-fold increase in signal while having an approximately 12-fold concentration increase in the coffee ring effect (Figure 1B) is the location of the electrodes. The edge of the droplet (contact line) is placed at the CE; although the CE and the WE are very close to each other, some of the molecules deposit on the CE. Nonetheless, the migration of the molecules toward the contact line increases the probability of the hybridization between the immobilized probes and target molecules. Notably, the coffee-ring effect also reduces the probe incubation time on the electrode, which was optimized to be 4 h in a humidified space, confirmed by electrochemical impedance spectroscopy (EIS) and SWV measurements (Figure S7). We also characterized the electrode surface topography and roughness using atomic force microscopy (AFM) in three different configurations: a bare gold electrode, a GNN-decorated electrode, and an electrode with viruses immobilized on it (Figure S8). AFM was used in tapping mode, incorporating a Multi75Al cantilever. The AFM measurements were performed in air. The electrodes were kept humidified in 0.1× PBS buffer right before the AFM measurement to minimize the non-specifically adsorbed particles. Comparing these three states in Figure S8 reveals that the roughness of the electrode surface increases in each step, confirming GNN deposition and virus capture on the electrode.

Tuning the Micro and Nanostructures. The GNN structures are made via two gold deposition steps: the first step uses an applied potential of 0 mV to generate out-of-plane microstructures on the electrode surface. The second step uses a more negative potential of −800 mV to promote the microelectrodes' nanostructuring. Here, we aimed to fine-tune the optimal micro- and nanostructuring of the electrodes for maximal current resolution in the ms range of the CA measurements. Figure 2A shows four examples of surface morphologies with different micro- and nanostructures. The overall surface area of the SPE/ring/GNN constructs that we generated in this work is about five times higher than our previously reported nanostructured micro-electrodes (NMEs),[18] and the anticipated capacitive and faradaic currents on these electrodes are expected to be higher depending on the electrode area and deposited amounts of molecular pendulums. As shown in Figure 2B,C, the CAMPA enhances signal resolution in all 4 structure levels; it is worth mentioning that the disc-like and ring-like electrodes possess the same surface area. The reason behind the difference between these two configurations is the coffee-ring effect. As most of the molecules in the evaporating droplet radially migrate toward the contact line, the probability of interaction between the target molecule and the immobilized probe is higher in the ring electrode with respect to the disc one.

Figure 2C shows that the optimal signal resolution is achievable with the third condition.

Simulation of the Preconcentration Process and Its Comparison with Experimental Data. To better understand the particle deposition rate during the preconcentration period, we simulated the viral-like particle deposition at the contact line of the ring electrodes, where the droplet pinning occurs, and compared it to the experimental data. The experimental analysis of the particle accumulation at the contact line shows that the concentration of the particles in the ring zone is around four times higher than their initial concentration in less than five min (Figure 3A). The images of the four time steps of the deposition

https://doi.org/10.1021/jacs.2c06192
J. Am. Chem. Soc. 2022, 144, 18338−18349

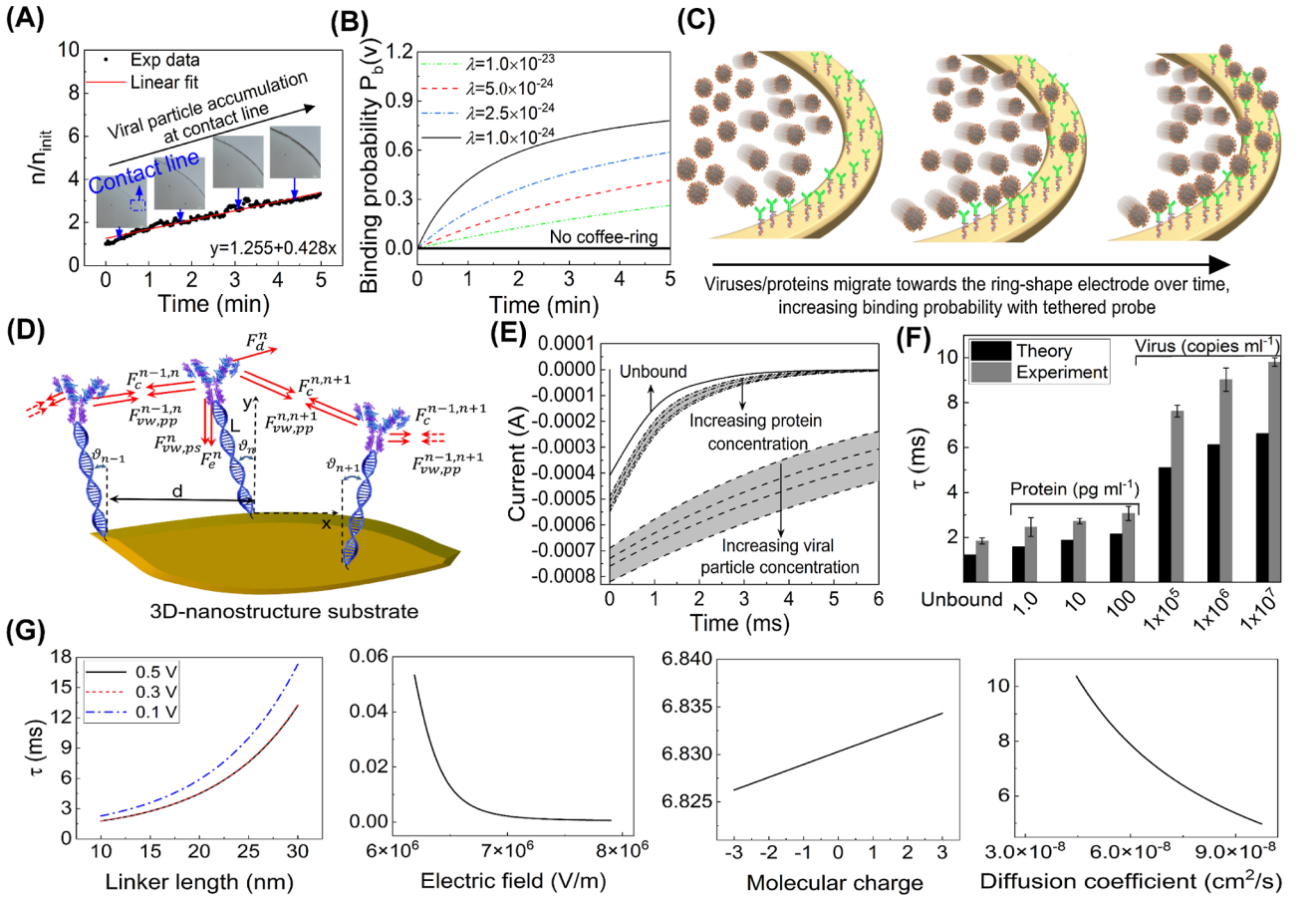

Figure 3. | Theoretical model of tethered NMPs vs. experimental observation. (A) Average distribution of the particles with the same size of the SARS-CoV-2 virus (~100 nm) at the contact line over time is used to monitor the fraction of particle accumulation as a result of the coffee-ring phenomenon. (B) Binding probability between the target molecule and the receptor protein over time with respect to no coffee-ring (NCR) state, calculated over time for different dissociation numbers. This shows that the coffee-ring effect increases the chance of binding from 20 to 80% in 5 min incubation. (C) Schematic of the process through which the coffee-ring phenomenon contributes to the interaction probability enhancement over time. (D) Parameters associated with the theoretical model. The tethered NMPs were dynamically modeled, taking into account the Stokes' drag force (F_d), the Lorentz force, the vertical force exerted by the applied field (F_e), the Van der Waals forces, distance-dependent interaction between proteins ($F_{vw,pp}$) and between the protein and the electrode surface ($F_{vw,ps}$), and the Coulomb force between the neighboring NMPs (F_c). The other variables incorporated in exploring the NMP dynamics are the length of the rigid linker (L), the distance (d), the angle of the NMPs to the surface (θ), the diffusion coefficient of the NMPs (D), and the molecular charge of NMPs (q). A positive electric field (E_{app}) is applied to the electrode to attract the negatively charged NMPs. All the parameters reflect the NMPs' transit time (τ) to reach the electrode surface, determined by solving the equations of motion (EOMs). (E) The simulated concentration-dependent current transients when exerting the electrode potential of 300 mV. The electrical current decays in case the NMP is bound to the two target molecular cargos in sizes of 10 nm (protein) and 100 nm (virus). The decay in the electrical current becomes slower by increasing the concentration of proteins or viruses. It is notable that the characteristic time is assumed to be in the form of $I_0e^{-t/\tau}$. (F) Comparison of calculated and observed τ values for various complexation states of the biosensor and various concentrations of N proteins and pseudotyped viruses (lentiviral particles display SARS-CoV-2 spike proteins). The experimental and theoretical data for N proteins and SARS-CoV-2 viruses for different concentrations are compared. (G) Effect of varying the linker length, electric field, molecular charge, and diffusion coefficient on the τ value, determined by the NMP dynamic simulation.

with approximately 1 min intervals (Figure 3A, middle) confirm the rapid increased concentration of the particles in the ring zone.

Proximity-Induced Binding Probability. As previously discussed, we hypothesized that the droplet pinning and coffee-ring formation of particles in the evaporation process lead to the increased sensitivity of our fabricated biosensor. Knowing the concentration of the target molecules at the contact line, the binding probability of the analyte with the tethered probes can be calculated by $P_b(V) \approx 1/[1 + (N_A\lambda/\alpha t)]$,[26] where N_A is Avogadro's constant, α is the slope of the concentration of particles versus time (calculated from Figure 3A), t represents time, λ is $\beta k_d/n_{init}$. k_d is the dissociation constant, and β is a constant parameter depending on the size of the control volume. The control volume is a cubic box in which proteins interact together. The box is considered to be at the top of the ring electrode with a width equal to the ring thickness. In this case, the target proteins enter the control volume over time due to the coffee-ring effect. Therefore, more particles come into the control volume over time, enhancing the binding probability (Figure 3B). Depending on the λ value, $P_b(V)$ increases over time at various rates, up to about 60% after 5 min compared to the no particle accumulation case (no coffee-ring). The underlying mechanism behind the $P_b(V)$ enhancement over time is the movement of target particles toward the edge of the ring where the molecular pendulums are immobilized (Figure 3C). It is worth mentioning that the thickness of the ring-shaped electrode affects the signal and should be optimized. To further

https://doi.org/10.1021/jacs.2c06192
J. Am. Chem. Soc. 2022, 144, 18338−18349

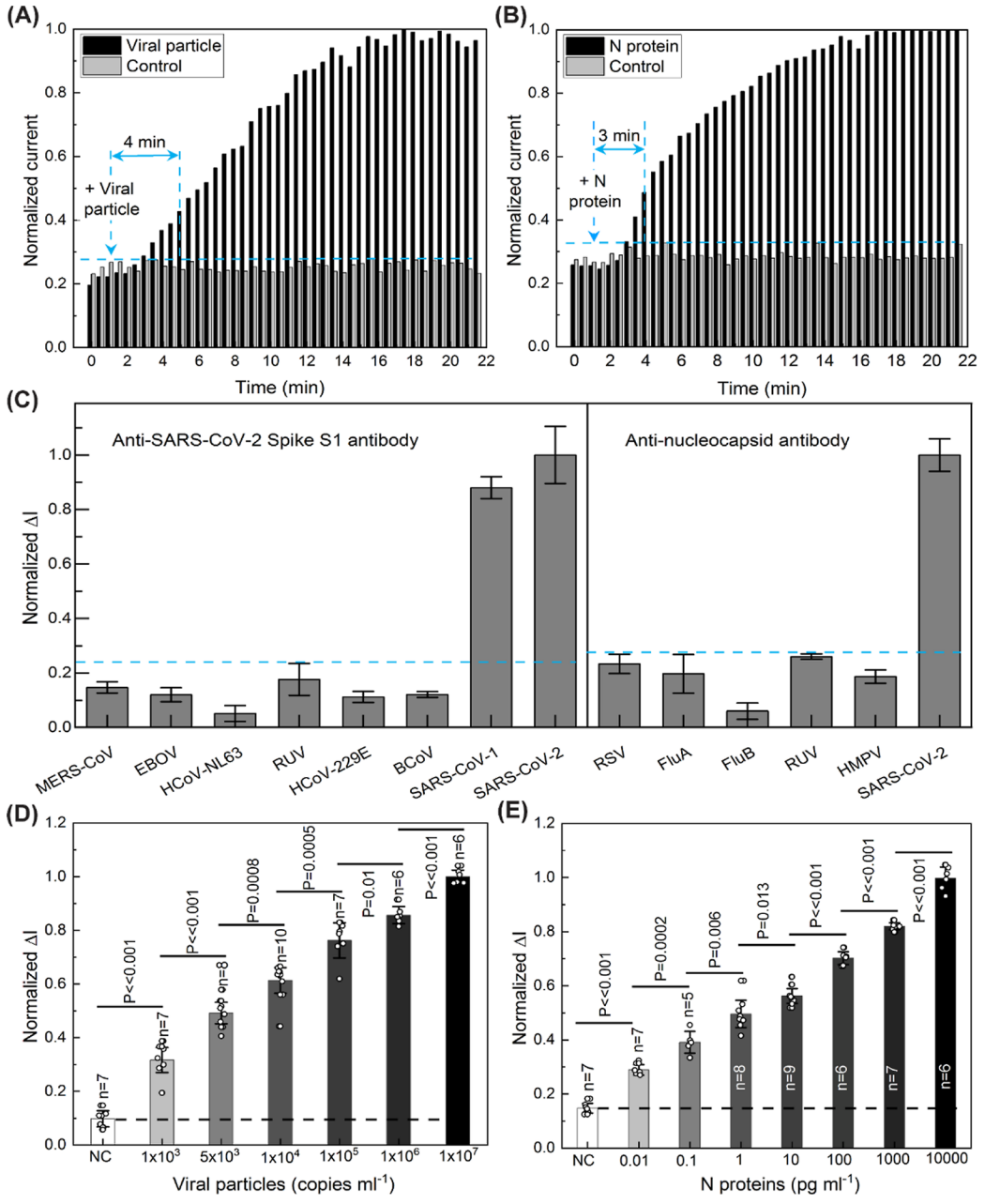

Figure 4. | Performance of capillary-assisted molecular pendulum assay (CAMPA) for protein and SARS-CoV-2 binding. (A) Comparing the time-dependent normalized current modulation in the presence and absence of pseudotyped viral particles bearing the SARS-CoV-2 spike proteins in a saliva sample. By adding the viral particles (5000 copies mL^{-1}) to the saliva sample after t = 1 min and performing the CA measurement every 30 s, it is shown that the sample is detectable in 4 min, and the system equilibrates in ∼15 min. (B) Comparing the time-dependent normalized current modulation in the presence and absence of N- protein in saliva samples illustrates the deviation in the measurable current associated with N-protein with respect to the control (IgG). The measurable current for N-protein (10 pg mL^{-1}) differentiates from control in 3 min and reaches a plateau within ∼15 min. The protein was injected into the sample at t = 1 min, and the signal was measured every 30 s using chronoamperometry (CA). The current magnitude is normalized by the maximum measured current. (C) Specificity of virus and N-protein detection. The tethered NMPs contain either an anti-SARS-CoV-2 Spike s1 antibody or an anti-Nucleocapsid antibody employed as recognition elements that can identify the SARS-CoV-2 s1 protein and N-protein with respect to the most common panel of viruses. A control line is set as a cut-off value representing the mean plus three times the standard deviation of the current alterations after incubating the biosensor for 20 min with the non-target proteins, Rubella (RuV), EBOV, HCoV-229E, HCoV-NL63, MERS-CoV, BCoV, and SARS-CoV-1 for anti-SARS-CoV-2 Spike s1 antibody and RSV, FluA, FluB, RuV, and HMPV for anti-Nucleocapsid antibody, in a buffer solution (n = 5). (D) Concentration-dependent signal alteration for pseudotyped viral particles in saliva. Subtracting the measured current for unbound and bound signals beyond the peak at 2 ms demonstrates that the limit of quantification (LoQ) extends down to 1000 copies mL^{-1}. (E), Concentration-dependent signal alteration for N-protein in saliva demonstrates that the LoQ extends down to 0.01 pg mL^{-1}. (C−E) Error bars show standard deviations with the center of mean value, and the measured current was normalized to its highest value. (D,E) Comparing the normalized currents for each concentration show that they are statistically significant from one another (P < 0.05; two-sided, two-sample t-tests).

https://doi.org/10.1021/jacs.2c06192
J. Am. Chem. Soc. 2022, 144, 18338−18349

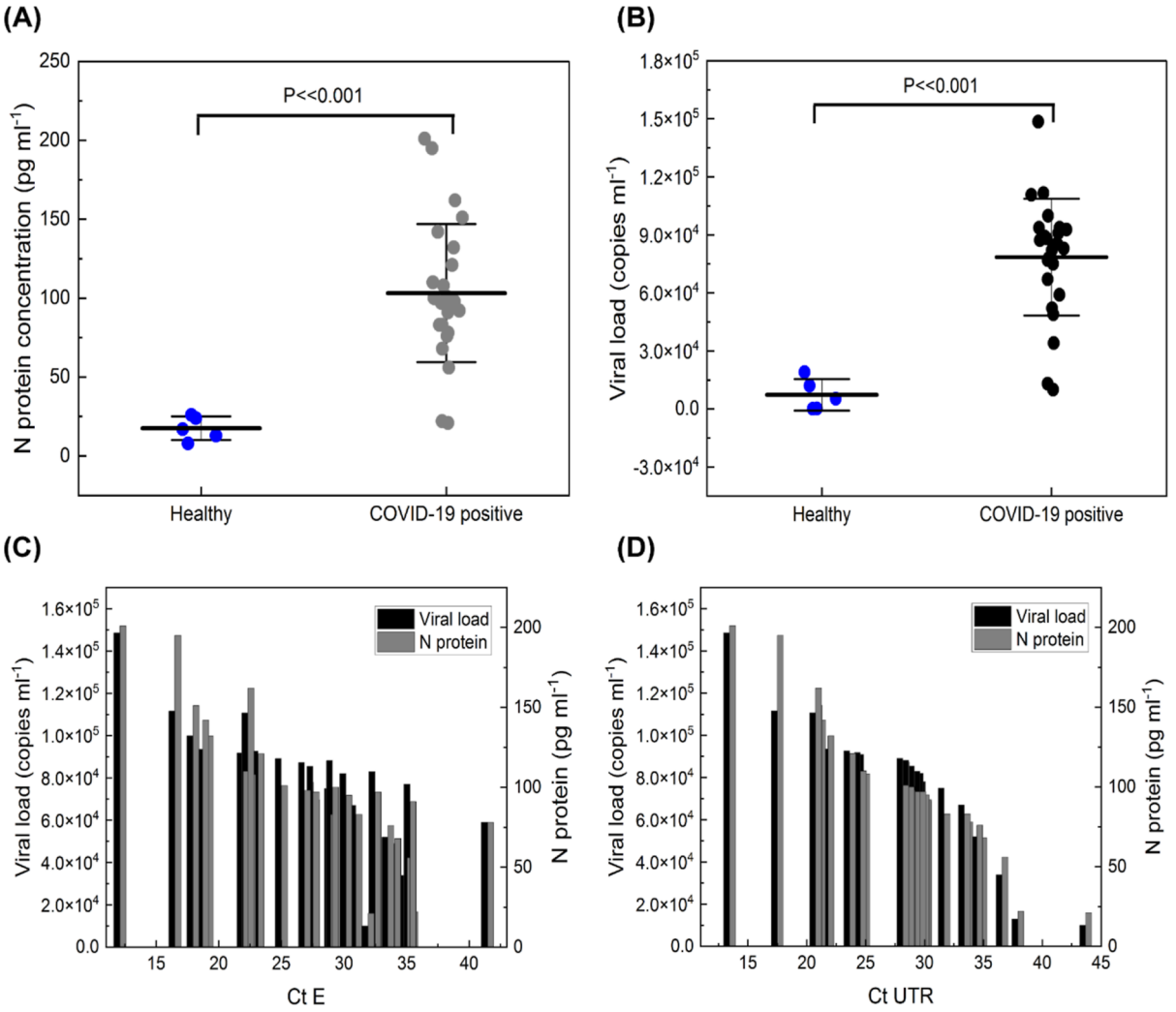

Figure 5. | Detection of SARS-CoV-2 virus and N protein in patient saliva samples. CAMPA biosensor for profiling of (A) nucleocapsid antigens and (B) SARS-CoV-2 virus in saliva samples collected from 30 participants who tested either COVID-19 negative ($n = 5$) or COVID-19 positive ($n = 25$). Statistically significant electrical currents are detected between positive and negative saliva samples ($P < 0.05$; two-sided, two-sample t-tests). (C−D) CAMPA results for profiling N-protein and viral loads are compared to UTR and E Ct values, calculated from reverse transcription polymerase chain reaction (RT-PCR) tests of patient samples. The results indicate that the viral load and N-protein concentrations are inversely proportional to both Ct values. The exception to this trend may be because of improper sample manipulation and storage, although there may still be no direct relationship between RNA concentration and viral load in some samples.

study the direct effects of the ring electrode thickness, we compared the electrode signals in bound and unbound configurations for electrodes with different ring thicknesses, from approximately 700 to 200 μm, as well as SPE250 electrodes (4 mm in diameter) without any treatment (Figure S1).

Molecular Pendulum Simulations versus Experiments. The NMPs used in this study were modeled as a monolayer of DNA probes spaced at a distance d apart and each of length L moving through angle θ (Figure 3D). The forces involved in the motion of the NMPs include a Lorentz force between the probe and electrode, a drag force tangential to the probe's pivoting arch, a Coulombic interaction between the probes in the monolayer, and van der Waals forces between neighboring probe proteins as well as between the proteins and the electrode. The equations of motion were derived for the NMPs (see Methods, "Formulized Model") and used to simulate the motion of NMPs and extract time-to-fall, τ, of unbound and bound biosensor configurations. The time-to-fall of each configuration was then fit to an exponential fitting in the form $I_0e^{-t/\tau}$to visualize the electrochemical current response. Increasing concentrations of both bound proteins and bound viral particles increase τ and lead to prolonged current responses (Figure 3E), with larger (>100 nm) viral particles having larger delays compared to proteins (<10 nm). Experimentally, τ is taken at 200 μs beyond the application of the step potential in chronoamperometry, and the τ values for numerous protein and viral particle concentrations were found to follow theoretical predictions (Figure 3F). We found out that the order of magnitude of the van der Waals forces is comparable with other forces, such as Stoke's drag and Coulombic interactions, and these forces are required to be considered in theoretical modeling. Having modified the model with van der Waals forces, we explored the contributions of probe parameters, including linker length, electric field, molecular charge, and diffusion coefficient (a function of analyte size). All parameter modifications, such as linker length, electric field, molecular charge, and diffusion coefficient, follow the trend expected as Lorentz force and drag force dominate probe motion, and the

https://doi.org/10.1021/jacs.2c06192
J. Am. Chem. Soc. 2022, 144, 18338−18349

contribution of van der Waals forces and Coulombic interactions impede motion in the monolayer (Figure 3G). Notably, other statistical theoretical models based on the experimental analysis of surface tethered ligands have been previously developed.[27−32] Our theoretical model is a depiction of a rigid rod with distally tethered mass using classical mechanics, rather than statistical mechanics. In this simplified approach, we treat the screening effect of DNA on the field by reducing the total charge by a factor of the relative permittivity of the electrolyte.[33] The benefits of modeling the kinetics of our system by considering equations of motion have allowed us to generate an intuitive representation of how ferrocene oxidation events are temporally related to bound protein size/mass/charge.

Detection of Nucleocapsid Proteins and Pseudotyped Viral Particles. To closely study the biosensors' detection time, we first spiked nucleocapsid (N) proteins and pseudotyped SARS-CoV-2 viral particles in the human saliva of healthy subjects. Alongside the negative controls (non-target proteins and non-target viral particles), we tested the biosensors by running CA every 30 s during their incubation with the samples. We showed that the biosensors detected viral particles in less than 4 min(Figure 4A) and N-proteins in less than 3 min(Figure 4B), while being fully stable under negative control samples. This observation agrees with our previously reported results of molecular pendulum sensors constructed on nanostructured electrodes;[18] however, in these experiments, we reduced probe incubation time in the functionalizing step, used low-cost SPEs, eliminating the need for a time-consuming and expensive process for making electrodes in cleanroom reported in our previous works, and designed more sensitive biosensors.

Characterization of Sensor Selectivity. We have examined the selective binding of the two molecular pendulum constructs made from anti-spike and anti-nucleocapsid protein antibodies with a panel of non-target proteins to demonstrate the selectivity of the biosensors to the target analyte. The selective binding of SARS-CoV-2 spike protein against MERS-CoV, EBOV, HCOV-NL63, RUV, HCoV-229E, and BCoV indicates that there is no significant alteration in the signal when non-specific molecules are present in the solution (Figure 4B, left). On the other hand, due to the unavoidable similarity of SARS-CoV-2 and SARS-CoV-1, the biosensors cannot differentiate between these two analytes. We also sought to confirm the selectivity of the nucleocapsid protein biosensors toward a panel of proteins related to other viral pathogens, such as RSV, Flu A, FluB, and HMPV, where these non-target proteins similarly produced no signal change upon exposure to nucleocapsid pendulums (Figure 4C, right).

Sensitivity and Calibration Curves. We can adjust our biosensors' sensitivity through two different approaches: (1) controlling the concentration of the molecular pendulum probe via alterations in probe deposition density and (2) changing the effective surface area of the electrode via controlling its nano- and microstructure. We fine-tuned these parameters to place the sensitivity range of the assay in line with the needed target concentration in clinical samples. Using spiked samples with known protein and viral particle concentrations, we correlated the target concentrations and the signals generated by the change in electrical current. Using the CAMPA approach, Figure 4D shows the limit of quantification (LOQ) for detection of viral particles in saliva to be 10^3 copies/mL, and Figure 4E shows the LOQ for detection of N-protein in saliva to be 100 fg/mL. The wide dynamic detection range of nucleocapsid protein (0.01−10,000 pg/mL) and viral particles (10^3−10^7 copies/mL) biosensors indicates the potential utility of the biosensors in the diagnosis of viral infections in their different stages. It is noteworthy that as the suspended molecules migrate to the droplet contact line from the middle part of the droplet, the increasing concentration of the target molecules saturates the probes placed closer to the droplet center, consequently decreasing the probability of hybridization with respect to lower target concentrations. In other words, the probes placed on the WE face target molecules from only one direction (radial), which causes a decrease in hybridization probability when increasing the target molecule concentration, which likely affects the sensitivity of the sensor in higher target molecule concentrations.

Processing of Clinical Samples. Moving from spiked saliva samples to patient saliva is a critical step that can bring variability to the experimental results. Therefore, it is important to demonstrate the functionality of biosensors in clinical samples. Using the calibration curves of Figure 4, we ran a blinded test on 25 patient saliva samples and determined their N-protein and viral load levels (Figure 5A,B). We then compared these results to their associated PCR values (Ct UTR and Ct E). Figure 5C,D shows higher Ct values when the protein/virus loads are low. Overall, the results show 93% agreement with the PCR data, which is an acceptable error for a rapid test.[34] It is noteworthy, however, that the saliva was diluted in these studies to normalize viscosity and increase sample volumes. Further work will be required to assess performance in unmanipulated specimens.

CONCLUSIONS

In this work, we introduce a cleanroom-free technique for the fabrication of ultrasensitive reagent-free electrochemical biosensors. We took advantage of the coffee-ring phenomenon in electrochemical biosensing for the first time to preconcentrate the target analytes for fast and sensitive detection of viral particles and proteins in SARS-CoV-2 samples. By exploiting the physics underlying an evaporating drop, we fabricated an optimized ring-shaped electrode to capture a high percentage of target molecules in a short period. Coffee-ring also offered reduced electrode preparation time due to the decreased probe incubation period. The feasibility of the work was studied theoretically and experimentally using spiked buffer and clinical patient samples. While representing high selectivity, the fabricated biosensors enabled the detection of N proteins and viral particles in less than 3 and 4 min, respectively. The clinical study asserts the accuracy of the biosensors for detecting the level of SARS-CoV-2 N protein and viral loads in patient saliva samples. This new generation of easy-to-use biosensors opens an avenue for affordable bioanalysis without compromising sensitivity, selectivity, and universality.

EXPERIMENTAL SECTION

Antibody Conjugation. An antibody−oligonucleotide conjugation kit [ab218260abcam Oligonucleotide Conjugation Kit (ab218260)] was used to conjugate antibody and amine-terminated DNA sequences with a 1:1 ratio.

Biosensor Fabrication. To obtain a ring-shaped electrode, gold screen-printed electrodes (SPE 250) were laser cut using a CO_2 laser cutter (Trotec SP500, Australia). The designed CAD file was first sketched in AutoCAD software (Autodesk, USA), and then the electrode was engraved, setting the power at 40%, speed at 12.7 cm/s, and PPI/Hz at 1000 to obtain the desired pattern. The resulting electrodes were electrochemically cleaned with 0.5 M H_2SO_4 using

https://doi.org/10.1021/jacs.2c06192
J. Am. Chem. Soc. 2022, 144, 18338−18349

cyclic voltammetry (CV) with a potential range of 0−1.1 V (vs Ag/AgCl) at a scan rate of 100 mV s^{-1} (30 cycles). The cleaned electrodes were decorated with gold (Au) nanoclusters in a solution of 0.1 mM L-cysteine, 0.1 M H_2SO_4, and 5 mM $HAuCl_4$ using chronoamperometry (CA) at a constant potential of 0 mV for 100 s. A fine Au nanocluster coating was formed on the Au structure during a second electrochemical deposition step in the same solution at a constant potential of −800 mV for various time windows, depending on the desired surface area and nanocluster morphology.

Biosensor Preparation. A thiolated probe solution (P1, 1 μM) in 1× PBS was added to 1 mM Tris(2-carboxyethyl) phosphine hydrochloride (TCEP) and incubated for an hour at room temperature in a dark chamber to reduce the protective disulfide bond. The P1 probe consists of a ferrocene redox reporter at 3′ end and a thiol group at the 5′ end. The P1 mixture was then heated to 55 °C for 5 min and cooled at room temperature. The antibody-conjugated complementary probe (P2, 1 μM) was added into the P1 solution and incubated for 10 min at room temperature to achieve hybridization. MCH solution was added into the P1−P2 probe mixture to a final concentration of 9 μM. A Western blot was used to ensure the conjugation of P1−P2 (Figure S9). The resulting mixture was then dropped onto the fabricated biosensor and incubated for 4 h at room temperature in a dark, humidified area to achieve the DNA probe immobilization. The functionalized biosensor was then washed, twice with a drop of 1× PBS for 5 min and one last time with a drop of 0.1× PBS. To keep the tethered DNA probe functional, the biosensors were kept immersed in 0.1× PBS buffer prior to the experiment. The samples were then incubated with the biosensors at room temperature for 10 min to complete the interaction of the target protein/virus and the tethered DNA probe. Following the incubation, the CA test was applied to the same solution without washing the biosensor.

Electrochemical Analysis. Electrochemical analyses were performed using a PGSTAT204 Potentiostat/Galvanostat (Metrohm-Autolab, Netherlands) instrument. Measurements were carried out on a modified screen-printed electrode containing a gold working electrode, silver reference electrode, and platinum auxiliary electrode. Electrochemical signals were measured by employing fast chronoamperometry (CA) utilizing a potential window from 0 to +300 mV versus Ag for 100 ms. The electrochemical results are based on the average of at least three replications. To characterize the electrodes, electrochemical impedance spectroscopy (EIS) and square wave voltammetry (SWV) were used. The EIS measurement was done within the frequency range of 0.1−10,000 Hz, with a potential amplitude of 14 mV versus the open circuit potential (Eocp) in $Fe(CN)_6^{3-/4-}$, containing 2.5 mM $K_3Fe(CN)_6$ and 2.5 mM $K_4Fe(CN)_6$, and 1× PBS buffer. EIS is carried out at various probe incubation times to find the optimized required time for probes to be properly immobilized on the surface of the electrode. SWV was also performed with the potential range of −100−500 mV, 4 mV step potential, amplitude 25 mV, and 60 Hz frequency in 0.1× PBS to evaluate the ferrocene peak.

Pseudotyped Virus Test. The process of producing viruses (Pseudotyping) is done following a common protocol detailed somewhere else.[35] Briefly, Pseudotyped lentiviruses were generated by transfecting 293T cells (a cell type engineered to express the SARS-CoV-2 receptor) with a lentiviral backbone plasmid.

Western Blot. We first lysed the Pseudotyped virus using a medium consisting of 1% SDS, with SARS-CoV-2 spike S1 protein utilized as a control. The resulting samples were added to a mixture of Bolt LDS sample buffer (catalog number B0007, Thermo Fisher Scientific) and 2.5% 2-mercaptoethanol. Prior to loading the solution, it was boiled at 70 °C for 10 min. Protein separation was achieved by applying a potential of 120 V for 1 to 1.5 h on 4−12% Bis-Tris gradient gels (catalog number NW04125BOX, Thermo Fisher Scientific) using MES SDS running buffer (catalog number NP0002, Thermo Fisher Scientific). It was then relocated from the gels to polyvinylidene difluoride (PVDF) membranes at 50 V for 2 h in Tris-Glycine buffer consisting of 10% methyl alcohol. We then blocked the PVDF membranes for 2 h at room temperature using Tris-buffered saline containing 0.1% Tween 20 (TBST) and 5% fat-free milk. Afterward, the membrane was probed with the primary antibody against Spike 1 protein (catalog number GTX135356, GeneTex) overnight at 4 °C. We then washed the membranes at least three times using TBST and incubated them at room temperature for 2 h with an anti-rabbit horseradish peroxidase-conjugated secondary antibody (catalog number 7074, Cell Signaling Technology, Inc). An enhanced chemiluminescence reagent (catalog number RPN2109, GE Health Care Canada, Inc.) was used to develop the band signals, visualized by a Bio-Rad gel imaging documentation system.

Patient Samples. The saliva samples of patients were collected from patients with laboratory-confirmed (RT-qPCR) COVID-19 by the Toronto Invasive Bacterial Diseases Network in metropolitan Toronto and the regional municipality of Peel in south-central Ontario, Canada (Research Ethics Board approvals studies #20−04 Unity Health Network, #02-0118-U/05-0016 C, Mount Sinai Hospital). To collect the saliva samples, Salivette tubes were utilized following manufacturer instructions (Sarstedt, Montreal, Quebec). The tube contains a cotton bud that the donor is instructed to chew for a certain period. The collected swab is relocated into an inner tube and transferred into an outer tube to extract liquid saliva using 3 min centrifugation at 1000g (Centrifuge 5910 R, Eppendorf). Saliva samples were previously tested for viral RNA 5′ untranslated region (UTR) gene and E gene using RT-PCR. We tested 30 patient samples, of which 25 were positive for the SARS-CoV-2 virus and 5 were negative for SARS-CoV-2. We diluted the samples with a 1:10 ratio using 0.1× PBS to improve the motility of virus/protein in the sample toward the working electrode under the coffee-ring phenomenon. No further sample preparation was needed. The diluted saliva was added to the biosensor for reagentless detection of the virus/protein. The patients' Ct value information is found in Table S1.

Formulized Model. The model in this study is based on our previous NMP work with some modifications.[17] Briefly, we formulized the biosensing process, considering the DNA and the target along with recognition elements as a rod and bob of an inverted pendulum, respectively. The rod that represents the double-stranded DNA is assumed to be rigid, and the bob has a spherical morphology.[17] A competition among drag, electrostatic, and van der Waals forces determines the difference between bound and unbound pendulums. The reason behind this difference is the noticeable effect of molecule/particle size on the rate of the pendulum motion at the micro-scale due to size-dependent drag and van der Waals forces. Although the electrochemical systems are commonly modeled through the statistical mechanics of free ions, we were able to theoretically model the system using classical mechanics, considering the sensing probes as tethered linkers in an electric field pivoting toward an electrode.[17]

Considering the charge (q), mass (m), and size (R) of the system concentrated into the bob, which is connected to the electrode surface through a rigid rod, the motion of the inverted pendulum was formulized.[17] The rod is fixed into the nanostructure surface, allowing it to pivot through all angles $-\pi/2 \leq \theta \leq \pi/2$ around the vertical axis.

The effective forces in a dense monolayer of the biosensor that play a crucial role in such a scale are the Lorentz force, which is directly applied to the charged bob; the van der Waals forces between neighboring bobs as well as a bob and electrode surface; the Stokes' drag force acting opposite to the relative angular motion of the pendulum; and the Coulombic interactions between adjacent charged bobs. The linkers are restricted to pivoting in the same range of θ due to the steric limitation.

The Gouy−Chapman approach was used to model the electric field in the bulk electrolyte, considering that there is no interaction between the monolayer and the static field formation. Assuming a 2D interaction between three linkers with an equal distance (d) and a periodic boundary condition, we solved the set of equations of motion (EOMs) for 50 nm × 50 nm discretized space. Adopting a grid size of 0.01 nm × 0.01 nm square cells for the computational simulation, the Gouy−Chapman potential was calculated along the vertical axis, y, utilizing the ensuing equation[36]

$$\varphi(y) = \frac{4k_BT}{ze} a \tan h\left[\tan h\left(\frac{ze\varphi_0}{4k_BT}\right)e^{-\kappa y}\right] \quad (1)$$

https://doi.org/10.1021/jacs.2c06192
J. Am. Chem. Soc. 2022, 144, 18338−18349

where z denotes the signed charge of the electrolyte, e is the electronic charge, φ_0 is the electrode potential, T denotes the absolute temperature, and k_B is the Boltzmann constant. The variable κ is calculated as

$$\kappa = \sqrt{\frac{2n^0 z^2 e^2}{\epsilon_r \epsilon_0 k_B T}} \tag{2}$$

in which ϵ_0 and ϵ_r are free space permittivity and relative permittivity of the electrolyte solution, respectively. The variable n^0 is the bulk concentration of the electrolyte per cubic meter, which is a function of molar concentration C_0 and Avogadro's number N_A: $n^0 = 1000 \times C_0 \times N_A$. The electric field is solved numerically by employing the finite difference method on $E = -d\varphi/dy$ in the discretized grid system.

Considering that the DNA probes form a monolayer on the nanocomposite, the effective forces that play a crucial role in this scale are Stokes' drag (F_d), Lorentz (F_e), Coulomb (F_c), van der Waals between proteins ($F_{vw,pp}$), and van der Waals between the protein and the electrode surface ($F_{vw,ps}$), defined as:

$$F_d = 6\pi\eta R\mathrm{v} \tag{3}$$

$$F_e = q'E \tag{4}$$

$$F_c = k_c \frac{q'q}{|r - r'|^3}(r - r') \tag{5}$$

$$F_{vw,pp} = -\frac{A}{6}\left\{\frac{2R^2}{(r - r')^2 - 4R^2} + \frac{2R^2}{(r - r')^2} + \ln\left(\frac{(r - r')^2 - 4R^2}{(r - r')^2}\right)\right\} \tag{6}$$

$$F_{vw,ps} = -\frac{A}{6}\left\{\frac{R}{z} + \frac{R}{2R + z} + \ln\left(\frac{z}{2R + z}\right)\right\} \tag{7}$$

in which R denotes the radius of the NMP's head, η is liquid viscosity, $r-r'$ is the spatial vector between two NMPs, K_c is the Coulomb's constant, q and q' are charges of the two neighbouring proteins, A is the Hamaker constant, and z is the nearest distance between protein and surface. Considering the Stokes–Einstein relation, the drag force can be rewritten as $F_d = k_B T v/D$, showing that the drag force is explicitly dependent on the diffusion coefficient (D) of the bob. Calculating the force balance in x and y directions, the equation of motion in cartesian coordinates can be described as

$$\begin{cases} m\ddot{x} = F_d^x + F_c^x + F_{vw,pp}^x \\ m\ddot{y} = F_d^y + F_c^y + F_e^y + F_{vw,pp}^y + F_{vw,ps}^y \end{cases} \tag{8}$$

Using the basic transformation, $x = l\sin\theta$ and $y = l\cos\theta$, the system can be formulized by θ. We evaluated the force balance for three neighboring NMPs labeled as n, $n + 1$, and $n - 1$. In this regard, the spatial vector between the two neighboring NMPs

$$r - r' = [2l^2 + d^2 + 2dl(\sin\theta_{i+1} - \sin\theta_i) - 2l^2\cos(\theta_{i+1} - \theta_i)]^{1/2}$$

and NMPs are at a distance d apart from each other. Considering a periodic boundary condition for the NMPs, the system of equations can be expressed as

$$\begin{cases} m l\ddot{\theta}_n = \dfrac{k_c q_n q_{n+1}(l\sin(\theta_n - \theta_{n+1}) - d\cos\theta_n)}{(r - r')^3} - \dfrac{k_c q_n q_{n-1}(l\sin(\theta_{n-1} - \theta_n) - d\cos\theta_n)}{(r - r')^3} - \dfrac{A(\cos\theta_n - \sin\theta_n)}{6}\left\{\dfrac{2R^2}{(r - r')^2 - 4R^2} + \dfrac{2R^2}{(r - r')^2} + \ln\left(\dfrac{(r - r')^2 - 4R^2}{(r - r')^2}\right)\right\} + \dfrac{A\sin\theta_n}{6}\left\{\dfrac{R}{l\cos\theta_n} + \dfrac{R}{2R + l\cos\theta_n} + \ln\left(\dfrac{l\cos\theta_n}{2R + l\cos\theta_n}\right)\right\} - 6\pi\eta R l\dot{\theta}_n - q_n E_y \sin\theta_n \\ m l\ddot{\theta}_{n+1} = \dfrac{k_c q_{n+1} q_{n-1}(l\sin(\theta_{n+1} - \theta_{n-1}) - d\cos\theta_{n+1})}{(r - r')^3} - \dfrac{k_c q_{n+1} q_n(l\sin(\theta_n - \theta_{n+1}) - d\cos\theta_{n+1})}{(r - r')^3} - \dfrac{A(\cos\theta_{n+1} - \sin\theta_{n+1})}{6}\left\{\dfrac{2R^2}{(r - r')^2 - 4R^2} + \dfrac{2R^2}{(r - r')^2} + \ln\left(\dfrac{(r - r')^2 - 4R^2}{(r - r')^2}\right)\right\} + \dfrac{A\sin\theta_{n+1}}{6}\left\{\dfrac{R}{l\cos\theta_{n+1}} + \dfrac{R}{2R + l\cos\theta_{n+1}} + \ln\left(\dfrac{l\cos\theta_{n+1}}{2R + l\cos\theta_{n+1}}\right)\right\} - 6\pi\eta R l\dot{\theta}_{n+1} - q_n E_y \sin\theta_{n+1} \\ m l\ddot{\theta}_{n-1} = \dfrac{k_c q_{n-1} q_n(l\sin(\theta_{n-1} - \theta_n) - d\cos\theta_{n-1})}{(r - r')^3} - \dfrac{k_c q_{n-1} q_{n+1}(l\sin(\theta_{n+1} - \theta_{n-1}) - d\cos\theta_{n-1})}{(r - r')^3} - \dfrac{A(\cos\theta_{n-1} - \sin\theta_{n-1})}{6}\left\{\dfrac{2R^2}{(r - r')^2 - 4R^2} + \dfrac{2R^2}{(r - r')^2} + \ln\left(\dfrac{(r - r')^2 - 4R^2}{(r - r')^2}\right)\right\} + \dfrac{A\sin\theta_{n-1}}{6}\left\{\dfrac{R}{l\cos\theta_{n-1}} + \dfrac{R}{2R + l\cos\theta_{n-1}} + \ln\left(\dfrac{l\cos\theta_{n-1}}{2R + l\cos\theta_{n-1}}\right)\right\} - 6\pi\eta R l\dot{\theta}_{n-1} - q_n E_y \sin\theta_{n-1} \end{cases} \tag{9}$$

The system of equations (eq 9) is transformed into the first-order differential equations considering the relation $\omega = \dot{\theta}$. The reduced form of eq 9 can be assessed like ordinary differential equations (ODE) and be solved employing the fourth-order Runge–Kutta method, which was programmed utilizing MATLAB. The theoretical time resolution is in the picosecond range, and the initial conditions of zero velocity of NMPs with various starting angles are considered. The code runs for each time step and stops once the nth DNA strand's bob reaches the biosensor's substrate (i.e., $y = 0$). We use the data from the nth DNA strand to perform further evaluations.

In actual practice, the ferrocene reporting molecule was attached at the distal end of the DNA NMP so that once the NMP touches the biosensor's surface, it produces a one-electron tunneling current. To mimic this behavior, a DNA linker is considered as the pendulum arm, and a bob plays the antibody role. In this case, we computationally assign 24 mer as the length of our NMPs (dsDNA pendulum arm), with an antibody of around 10 nm diameter and a size of 150 kDa, like an immunoglobulin-G (IgG)-formatted antibody. The size and pl of the analyte are estimated based on the short- and long-axis protein lengths utilizing available database knowledge through UniProt and the contribution of its charge from PhosphoSite, respectively. The size of the virus is also considered to be around 100 nm. Detailed information regarding the parameters in the theoretical study can be found in the Supporting Information (Table S2).

Considering NMPs with random starting angles, we solved eq 9. The characteristic time of the system for the average τ can be utilized as an estimation of the decay rate of the electron transfer in the defined system. In the linear time-invariant (LTI) system, we can consider the τ value as the typical time through which the output of electron-transfer relates to electrical current using the formula $I(t) = I_0 e^{-t/\tau} = I_0 e^{-k_{eff}t}$. Here, $k_{eff} = 1/\tau$ denotes the effective electron transfer rate. k_{eff} can be theoretically determined by averaging the calculated τ value of target molecules using random primary angles. The k_{eff} value can be determined using experimental data by exponentially fitting the portion of data that is decayed in the fast chronoamperometry test. It can also be calculated by reciprocating the time where the peak current is 1/e

https://doi.org/10.1021/jacs.2c06192
J. Am. Chem. Soc. 2022, 144, 18338–18349

(36.8%) of its value, which, in linear time-invariant cases, is considered as the characteristic time.

Materials. DNA sequences, 5′−SH−MC6-TAC CAG CTA TTG TAT CTA ATA AGA-Fc-3′ (P1) and 5′-NH2-C6-TCT TAT TAG ATA CAA TAG CTG GTA (P2), were purchased from Integrated DNA Technologies (IDT). Ferrocene NHS ester was purchased from Five Photon Biochemicals. SARS-CoV-2 Nucleocapsid Antibody (NBP3-05730) Recombinant Virus and SARS-CoV-2 Nucleocapsid Protein (NBP2-90975) were obtained from Cedarlane. The anti-SARS-CoV-2 spike S1 antibody was obtained from the Rini Lab at the University of Toronto. Ebola virus (EBoV) (40442-V08H4), human coronavirus (HCoV-229E) spike/s1 protein (40601-V08H), human coronavirus (HCoV-NL63) spike protein (S1 + S2 ECD, 40604-V08B), MERS coronavirus (MERS-CoV) spike protein (S1 + S2 ECD, aa 1-1297, 40069-V08B), and SARS-CoV-2 (2019-nCoV) spike S1 protein (40591-V08H) were obtained from Sino Biological Inc. Recombinant Rubella Virus (RuV) spike glycoprotein E1 protein (Fc Chimera, ab256429), bovine coronavirus spike glycoprotein (BCoV, ab235851), and recombinant SARS spike glycoprotein (Coronavirus, SARS-CoV-1, ab49046) were purchased from Abcam. The pseudotyped virus was obtained from the Cochrane lab at the University of Toronto. Gold screen-printed electrodes, model SPE250, were obtained from Metrohm, Canada. Sulfuric acid (H_2SO_4), TCEP, and 6-Mercapto-1-hexanol (MCH) were purchased from Sigma-Aldrich. Potassium ferrocyanide ($K_4[Fe(CN)_6]$) and potassium ferricyanide ($K_3[Fe(CN)_6]$) were obtained from Merck (Germany). UltraPure DNase/RNase-Free Distilled Water and Sterile PBS were purchased from Wisent Bioproducts. Human saliva solution was purchased from Lee Biosolutions. Patient saliva samples collected from volunteers were provided by Dr. Samira Mubareka (Sunnybrook Research Institute) and Dr. Allison McGeer (Mount Sinai Hospital). SYBR Gold nucleic acid gel stain, Invitrogen Ambion Gel Loading Buffer II, and DNase were purchased from Thermo Scientific. 40% polyacrylamide solution, nonionic water-soluble polymer with a 29:1 ratio, and Urea (ultrapure) were purchased from BioShop Canada (Burlington, ON, Canada).

■ ASSOCIATED CONTENT

Supporting Information

The Supporting Information is available free of charge at https://pubs.acs.org/doi/10.1021/jacs.2c06192.

Effect of electrode shape on transition time in the unbound and bound states; the study of contact line pinning of a saliva sample drop casted on the electrode using DSA; electrode cleaning and stability using CV; SWV for the unbound and bound states in 1x PBS; probe incubating time optimization; electrode's surface topography in different configurations characterized using AFM; western blot analysis representing the conjugation of the DNA probe and antibody; the UTR and E Ct values of SARS-CoV-2 positive or negative patient saliva samples; and model parameters for designing molecular pendulum simulation (PDF)

■ AUTHOR INFORMATION

Corresponding Authors

Amir Sanati Nezhad − *Department of Mechanical and Manufacturing Engineering, University of Calgary, Calgary, Alberta T2N 1N4, Canada;* orcid.org/0000-0002-2309-2388; Email: amir.sanatinezhad@ucalgary.ca

Shana O. Kelley − *Leslie Dan Faculty of Pharmacy, University of Toronto, Toronto, ON M5S 3M2, Canada; Department of Chemistry, Northwestern University, Evanston, Illinois 60208, United States; Department of Biomedical Engineering, Northwestern University, Evanston, Illinois 60208, United States; Department of Biochemistry and Molecular Genetics, Northwestern University, Chicago, Illinois 60611, United States;* orcid.org/0000-0003-3360-5359; Email: shana.kelley@utoronto.ca

Authors

Hossein Zargartalebi − *Department of Mechanical and Manufacturing Engineering, University of Calgary, Calgary, Alberta T2N 1N4, Canada; Leslie Dan Faculty of Pharmacy, University of Toronto, Toronto, ON M5S 3M2, Canada*

Hanie Yousefi − *Leslie Dan Faculty of Pharmacy, University of Toronto, Toronto, ON M5S 3M2, Canada*

Connor D. Flynn − *Department of Chemistry, Northwestern University, Evanston, Illinois 60208, United States; Department of Chemistry, University of Toronto, Toronto, ON M5S 3M2, Canada*

Surath Gomis − *The Edward S. Rogers Sr. Department of Electrical and Computer Engineering, University of Toronto, Toronto, ON M5S 3G4, Canada*

Jagotamoy Das − *Department of Chemistry, Northwestern University, Evanston, Illinois 60208, United States;* orcid.org/0000-0003-2724-1827

Tiana L. Young − *Leslie Dan Faculty of Pharmacy, University of Toronto, Toronto, ON M5S 3M2, Canada;* orcid.org/0000-0001-7527-811X

Emily Chien − *Sunnybrook Research Institute, Toronto, ON M4N 3N5, Canada*

Samira Mubareka − *Sunnybrook Research Institute, Toronto, ON M4N 3N5, Canada*

Allison McGeer − *Department of Microbiology, Sinai Health System, Toronto, ON M5G 1X5, Canada*

Hansen Wang − *Leslie Dan Faculty of Pharmacy, University of Toronto, Toronto, ON M5S 3M2, Canada*

Edward H. Sargent − *The Edward S. Rogers Sr. Department of Electrical and Computer Engineering, University of Toronto, Toronto, ON M5S 3G4, Canada;* orcid.org/0000-0003-0396-6495

Complete contact information is available at: https://pubs.acs.org/10.1021/jacs.2c06192

Author Contributions

H.Z. and H.Y. contributed equally. The manuscript was written through the contributions of all the authors. All authors have given approval to the final version of the manuscript.

Notes

The authors declare no competing financial interest.

■ ACKNOWLEDGMENTS

We would like to acknowledge all the patients who generously contributed specimens for testing as well as Prof. Alan Cochrane for sharing the pseudotyped lentiviral particles.

■ ABBREVIATIONS

CA	chronoamperometry
CV	cyclic voltammetry
SWV	square wave voltammetry
AFM	atomic force microscopy
SEM	scanning electron microscope
RuV	Rubella virus
EBOV	Ebola virus
HCoV-229E	Human Corona virus (strain 229E)
HCoV-NL63	Human Corona virus (strain NL63)
MERS-CoV	middle east respiratory syndrome Corona virus
BCoV	bovine Corona virus

SPE	screen-printed electrode
SARS CoV-2	severe acute respiratory syndrome coronavirus 2
NMP	nanoscale molecular pendulum
GNN	gold nanoneedles
CAMPA	capillary-assisted molecular pendulum assay

REFERENCES

(1) Luong, J. H.; Male, K. B.; Glennon, J. D. Biosensor technology: technology push versus market pull. *Biotech. Adv.* **2008**, *26*, 492−500.

(2) Cinti, S.; Moscone, D.; Arduini, F. Preparation of paper-based devices for reagentless electrochemical (bio) sensor stripsPreparation of paper-based devices for reagentless electrochemical (bio)sensor strips. *Nat.Prot.* **2019**, *14*, 2437−2451.

(3) Hönes, J.; Müller, P.; Surridge, N. Therapeutics, The technology behind glucose meters: test strips. *Diab. Tech.* **2008**, *10*, S10−26.

(4) Koczula, K. M.; Gallotta, A. Lateral flow assays. *Essays Biochem.* **2016**, *60*, 111−120.

(5) Mahmoudi, T.; de la Guardia, M.; Shirdel, B.; Mokhtarzadeh, A.; Baradaran, B. Recent advancements in structural improvements of lateral flow assays towards point-of-care testing. *TrAC Trends Anal. Chem.* **2019**, *116*, 13−30.

(6) Jalandra, R.; Yadav, A. K.; Verma, D.; Dalal, N.; Sharma, M.; Singh, R.; Kumar, A.; Solanki, P. R. Strategies and perspectives to develop SARS-CoV-2 detection methods and diagnostics. *Biomed, Pharmacother.* **2020**, *129*, 110446.

(7) Valera, E.; Jankelow, A.; Lim, J.; Kindratenko, V.; Ganguli, A.; White, K.; Kumar, J.; Bashir, R. COVID-19 point-of-care diagnostics: present and future. *ACS Nano* **2021**, *15*, 7899−7906.

(8) Rasmi, Y.; Li, X.; Khan, J.; Ozer, T.; Choi, J. R. Emerging point-of-care biosensors for rapid diagnosis of COVID-19: current progress, challenges, and future prospects. *Anal. Bioanal. Chem.* **2021**, *413*, 4137−4159.

(9) Giri, B.; Pandey, S.; Shrestha, R.; Pokharel, K.; Ligler, F. S.; Neupane, B. B. Review of analytical performance of COVID-19 detection methods. *Anal. Bioanal. Chem.* **2021**, *413*, 35−48.

(10) Scohy, A.; Anantharajah, A.; Bodéus, M.; Kabamba-Mukadi, B.; Verroken, A.; Rodriguez-Villalobos, H. Low performance of rapid antigen detection test as frontline testing for COVID-19 diagnosis. *J. Clin. Virol.* **2020**, *129*, 104455.

(11) Torrente-Rodríguez, R. M.; Lukas, H.; Tu, J.; Min, J.; Yang, Y.; Xu, C.; Rossiter, H. B.; Gao, W. SARS-CoV-2 RapidPlex: a graphene-based multiplexed telemedicine platform for rapid and low-cost COVID-19 diagnosis and monitoring. *Matter* **2020**, *3*, 1981−1998.

(12) Alafeef, M.; Dighe, K.; Moitra, P.; Pan, D. Rapid, ultrasensitive, and quantitative detection of SARS-CoV-2 using antisense oligonucleotides directed electrochemical biosensor chip. *ACS Nano* **2020**, *14*, 17028−17045.

(13) Norman, M.; Gilboa, T.; Ogata, A. F.; Maley, A. M.; Cohen, L.; Busch, E. L.; Lazarovits, R.; Mao, C.-P.; Cai, Y.; Zhang, J.; Feldman, J. E.; Hauser, B. M.; Caradonna, T. M.; Chen, B.; Schmidt, A. G.; Alter, G.; Charles, R. C.; Ryan, E. T.; Walt, D. R. Ultrasensitive high-resolution profiling of early seroconversion in patients with COVID-19. *Nat. Biomed. Eng.* **2020**, *4*, 1180−1187.

(14) Ter-Ovanesyan, D.; Gilboa, T.; Lazarovits, R.; Rosenthal, A.; Yu, X.; Li, J. Z.; Church, G. M.; Walt, D. R. Ultrasensitive measurement of both SARS-CoV-2 RNA and antibodies from saliva. *Anal. Chem.* **2021**, *93*, 5365−5370.

(15) Seo, G.; Lee, G.; Kim, M. J.; Baek, S.-H.; Choi, M.; Ku, K. B.; Lee, C.-S.; Jun, S.; Park, D.; Kim, H. G.; Kim, S.-J.; Lee, J.-O.; Kim, B. T.; Park, E. C.; Kim, S. I. Rapid detection of COVID-19 causative virus (SARS-CoV-2) in human nasopharyngeal swab specimens using field-effect transistor-based biosensor. *ACS Nano* **2020**, *14*, 5135−5142.

(16) Ning, B.; Yu, T.; Zhang, S.; Huang, Z.; Tian, D.; Lin, Z.; Niu, A.; Golden, N.; Hensley, K.; Threeton, B.; Lyon, C. J.; Yin, X. M.; Roy, C. J.; Saba, N. S.; Rappaport, J.; Wei, Q.; Hu, T. Y. A smartphone-read ultrasensitive and quantitative saliva test for COVID-19. *Sci. Adv.* **2021**, *7*, No. eabe3703.

(17) Das, J.; Gomis, S.; Chen, J. B.; Yousefi, H.; Ahmed, S.; Mahmud, A.; Zhou, W.; Sargent, E. H.; Kelley, S. O. Reagentless biomolecular analysis using a molecular pendulum. *Nat. Chem.* **2021**, *13*, 428−434.

(18) Yousefi, H.; Mahmud, A.; Chang, D.; Das, J.; Gomis, S.; Chen, J. B.; Wang, H.; Been, T.; Yip, L.; Coomes, E.; Li, Z.; Mubareka, S.; McGeer, A.; Christie, N.; Gray-Owen, S.; Cochrane, A.; Rini, J. M.; Sargent, E. H.; Kelley, S. O. Detection of SARS-CoV-2 viral particles using direct, reagent-free electrochemical sensing. *J. Am. Chem. Soc.* **2021**, *143*, 1722−1727.

(19) La Colla, N. S.; Domini, C. E.; Marcovecchio, J. E.; Botté, S. E. Latest approaches on green chemistry preconcentration methods for trace metal determination in seawater−a review. *J. Environ. Mgmt.* **2015**, *151*, 44−55.

(20) Khnouf, R.; Han, C. Isotachophoresis-Enhanced Immunoassays: Challenges and opportunities. *IEEE Nanotechnol. Mag.* **2020**, *14*, 6−17.

(21) Deegan, R. D.; Bakajin, O.; Dupont, T. F.; Huber, G.; Nagel, S. R.; Witten, T. A. Capillary flow as the cause of ring stains from dried liquid drops. *Nature* **1997**, *389*, 827−829.

(22) Yunker, P. J.; Still, T.; Lohr, M. A.; Yodh, A. Suppression of the coffee-ring effect by shape-dependent capillary interactions. *Nature* **2011**, *476*, 308−311.

(23) Zargartalebi, H.; Hejazi, S. H.; Sanati-Nezhad, A. Self-assembly of highly ordered micro-and nanoparticle deposits. *Nature Comm* **2022**, *13*, 1−11.

(24) Mampallil, D.; Eral, H. B. A review on suppression and utilization of the coffee-ring effect. *Adv. Coll. Inter. Sci.* **2018**, *252*, 38−54.

(25) Chen, J. B.; Yousefi, H.; Nemr, C. R.; Gomis, S.; Atwal, R.; Labib, M.; Sargent, E.; Kelley, S. O. Nanostructured architectures for biomolecular detection inside and outside the cell. *Adv. Func. Mater.* **2020**, *30*, 1907701.

(26) Jost Lopez, A.; Quoika, P. K.; Linke, M.; Hummer, G.; Köfinger, J. r. Quantifying protein−protein interactions in molecular simulations. *J. Phys. Chem. C* **2020**, *124*, 4673−4685.

(27) Knezevic, J.; Langer, A.; Hampel, P. A.; Kaiser, W.; Strasser, R.; Rant, U. Quantitation of affinity, avidity, and binding kinetics of protein analytes with a dynamically switchable biosurface. *J. Am. Chem. Soc.* **2012**, *134*, 15225−15228.

(28) Sendner, C.; Kim, Y. W.; Rant, U.; Arinaga, K.; Tornow, M.; Netz, R. Dynamics of end grafted DNA molecules and possible biosensor applications. *Physica Status Solid* **2006**, *203*, 3476−3491.

(29) Rant, U.; Pringsheim, E.; Kaiser, W.; Arinaga, K.; Knezevic, J.; Tornow, M.; Fujita, S.; Yokoyama, N.; Abstreiter, G. Detection and size analysis of proteins with switchable DNA layers. *Nano Lett.* **2009**, *9*, 1290−1295.

(30) Langer, A.; Hampel, P. A.; Kaiser, W.; Knezevic, J.; Welte, T.; Villa, V.; Maruyama, M.; Svejda, M.; Jähner, S.; Fischer, F. Protein analysis by time-resolved measurements with an electro-switchable DNA chip. *Nature Comm* **2013**, *4*, 1−8.

(31) Langer, A.; Kaiser, W.; Svejda, M.; Schwertler, P.; Rant, U. Molecular dynamics of DNA−protein conjugates on electrified surfaces: solutions to the drift-diffusion equation. *J. Phys. Chem. B* **2014**, *118*, 597−607.

(32) Kroener, F.; Heerwig, A.; Kaiser, W.; Mertig, M.; Rant, U. Electrical actuation of a DNA origami nanolever on an electrode. *J. Am. Chem. Soc.* **2017**, *139*, 16510−16513.

(33) Maffeo, C.; Yoo, J.; Comer, J.; Wells, D.; Luan, B.; Aksimentiev, A. Close encounters with DNA. *J. Phys.: Cond. Matt.* **2014**, *26*, 413101.

(34) Vandenberg, O.; Martiny, D.; Rochas, O.; van Belkum, A.; Kozlakidis, Z. Considerations for diagnostic COVID-19 tests. *Nat. Rev. Microbiol.* **2021**, *19*, 171−183.

(35) Crawford, K. H.; Eguia, R.; Dingens, A. S.; Loes, A. N.; Malone, K. D.; Wolf, C. R.; Chu, H. Y.; Tortorici, M. A.; Veesler, D.; Murphy, M.; Pettie, D.; King, N. P.; Balazs, A. B.; Bloom, J. D. Protocol and reagents for pseudotyping lentiviral particles with SARS-CoV-2 spike protein for neutralization assays. *Viruses* **2020**, *12*, 513.

(36) Faulkner, L. R.; Bard, A. J. *Electrochemical Methods: Fundamentals and Applications*; John Wiley and Sons, 2002.

https://doi.org/10.1021/jacs.2c06192
J. Am. Chem. Soc. 2022, 144, 18338−18349